SCIENCE CHINA
Technological Sciences

November 2010 Vol.53 No.11: 2954–2959
doi: 10.1007/s11431-010-4140-z

Numerical simulation on drag reduction of revolution body through bionic riblet surface

ZHANG ChengChun[1], WANG Jing[1,2*] & SHANG YanGeng[1]

[1] *Key Laboratory of Bionics Engineering, Ministry of Education, Jilin University, Changchun 130022, China;*
[2] *College of Agriculture, Department of Physics, Jilin University, Changchun 130062, China*

Received August 7, 2010; accepted August 24, 2010

Numerical simulations of flow fields on the bionic riblet and the smooth revolution bodies were performed based on the SST k-ω turbulence model in order to explain the mechanisms of the skin friction drag reduction, base drag reduction on the riblet surface, and flow control behaviors of riblet surface near the wall. The simulation results show that the riblet surface arranged on the rearward of the revolution body can reduce the skin friction drag by 8.27%, the base drag by 9.91% and the total drag by 8.59% at *Ma* number 0.8. The riblet surface reduces the skin friction drag by reducing the velocity gradient and turbulent intensity, and reduces the base drag by weakening the pumping action on the dead water region which behind the body of revolution caused by the external flow. The flow control behavior on boundary layer shows that the riblet surface can cut the low-speed flow near the wall effectively, and restrain the low-speed flow concentrating in span direction, thus weaken the instability of the low speed steaks produced by turbulent flow bursting.

bionic engineering, riblet surface, drag reduction, numerical simulation, revolution body

Citation: Zhang C C, Wang J, Shang Y G. Numerical simulation on drag reduction of revolution body through bionic riblet surface. Sci China Tech Sci, 2010, 53: 2954–2959, doi: 10.1007/s11431-010-4140-z

1 Introduction

Bionic researches found that the animals living in fluid environment had evolved unique non-smooth surfaces and unconventional structures with drag reduction function after a long-term evolution. Results of previous researches showed that the riblet surface of shark skin can reduce the swimming drag [1–4]. Fish and Battle [5], and Miklosovic [6] found that the large protuberances or tubercles located on the leading edge of humpback whale flipper can increase lift and decrease drag. Anderson et al. [7] found that scallop shells exhibit optimization of riblet dimensions for drag reduction. Many researchers explored the drag reduction mechanisms of the riblet surface by using experiments, numerical simulation and theoretical analysis. Luchini et al. [8] suggested that riblet surface can hamper the lateral component of the near-wall flow, and reduce momentum transfer and wall shear stress. Choi et al. [9], Wang et al. [10] and Goldstein et al. [11] supported this view by experimental and numerical investigations.

Most of the researches were performed only to reduce the surface friction drag. But for the revolution body, the pressure drag has an important effect on the aerodynamic drag. Our previous researches examined the drag reductions of bodies of revolution with riblet surface and dimpled surface by using wind tunnel tests. The results confirmed that the bionic surface could reduce not only the skin friction drag but also the pressure drag [12, 13]. However, it is difficult to explore the mechanism of drag reduction using experiments only. Therefore, in this paper, we conducted a comparison analysis of external flow between two revolution

*Corresponding author (email: jluzcc@jlu.edu.cn)

bodies of smooth surface and riblet surface, respectively. By numerical simulations with the SST k-ω turbulence model, the mechanism of drag reduction of the riblet surface for viscous drag was explored and pressure drag was discussed.

2 Modeling approach

2.1 Governing equation

The governing equation can be written in the compact universal form:

$$\frac{\partial(\rho\phi)}{\partial t}+\operatorname{div}(\rho u\phi)=\operatorname{div}\left(\Gamma_\phi \operatorname{grad}\phi\right)+S_\phi. \tag{1}$$

Table 1 shows the concrete terms of eq. (1) for a compressible steady state flow.

2.2 Turbulence modeling

The two-equation turbulence models are now widely used in engineering application, due to their good compromise between numerical effort and computational accuracy. The shear-stress transport (SST) k-ω model, developed by Menter [14], is used for fully turbulent simulations, which can effectively blend the robust and accurate formulation of the k-ω model (in the near-wall region) with the free-stream independence of the k-ε model (in the far field). For the transonic flows, the SST k-ω model has shown the best compromise between the physical capabilities and the numerical stiffness [15]. The transport equations governing k and ω take the following form without regarding to the buoyancy:

$$\frac{\mathrm{d}(\rho k)}{\mathrm{d}t}=\tau_{ij}\frac{\partial u_i}{\partial x_j}+\frac{\partial}{\partial x_j}\left[\left(\mu+\sigma_k\mu_t\right)\frac{\partial k}{\partial x_j}\right]-\beta^*\rho\omega k, \tag{2}$$

$$\begin{aligned}\frac{\mathrm{d}(\rho\omega)}{\mathrm{d}t}=&\frac{\gamma\rho}{\mu_t}\tau_{ij}\frac{\partial u_i}{\partial x_j}+\frac{\partial}{\partial x_j}\left[\left(\mu+\sigma_\omega\mu_t\right)\frac{\partial\omega}{\partial x_j}\right]\\&-\beta\rho\omega^2+2\rho(1-F_1)\sigma_{\omega2}\frac{1}{\omega}\frac{\partial k}{\partial x_j}\frac{\partial\omega}{\partial x_j},\end{aligned} \tag{3}$$

Table 1 The concrete terms of governing equation of flow for a compressible fluid

Equation	Terms		
	ϕ	Γ_ϕ	S_ϕ
Continuity	1	0	0
Momentum	u_i	μ	$-\frac{\partial p}{\partial x_i}+S_i$
Energy	T	$\frac{k}{c}$	S_T

where τ_{ij} is the turbulent shear stress. The production term of τ_{ij} in eq. (2) and eq. (3) is

$$\tau_{ij}\frac{\partial u_i}{\partial x_j}=\mu_t\left[S_{ij}^2-\frac{2}{3}\left(\frac{\partial u_k}{\partial x_k}\right)^2-\frac{2}{3}\rho k\frac{\partial u_k}{\partial x_k}\right]. \tag{4}$$

The blending functions F_1 and F_2 are defined as

$$F_1=\tanh(\arg_1^4), \tag{5}$$

$$F_2=\tanh(\arg_2^2), \tag{6}$$

where

$$\arg_1=\min\left[\max\left(\frac{\sqrt{k}}{0.09\omega y},\frac{500\mu}{\rho y^2\omega}\right),\frac{4\rho k\sigma_{\omega2}}{CD_{k\omega}y^2}\right], \tag{7}$$

$$CD_{k\omega}=\max\left(2\rho\sigma_{\omega2}\frac{1}{\omega}\frac{\partial k}{\partial x_j}\frac{\partial\omega}{\partial x_j},10^{-20}\right), \tag{8}$$

$$\arg_2=\max\left(2\frac{\sqrt{k}}{0.09\omega y},\frac{500\mu}{\rho y^2\omega}\right). \tag{9}$$

The turbulent eddy viscosity can be calculated by the following formula:

$$\mu_t=\frac{\rho a_1 k}{\max(a_1\omega,\Omega F_2)}. \tag{10}$$

The model constants can be calculated by using the F_1 blending function:

$$\phi=F_1\phi_1+(1-F_1)\phi_2, \tag{11}$$

where ϕ_1 represents a generic constant in the k-ω equations and ϕ_2 represents the same constant in the k-ε equations.

The k-ω model constants are given by

$$\sigma_{k1}=0.85,\sigma_{\omega1}=0.5,\beta_1=0.0750,\gamma=\frac{\beta_1}{\beta^*}-\frac{\sigma_{\omega1}\kappa^2}{\sqrt{\beta^*}},$$

$$\kappa=0.41,\beta^*=0.09,a_1=0.31.$$

The values of k-ε model constants are

$$\sigma_{k2}=1.0,\sigma_{\omega2}=0.856,\beta_2=0.0828,\gamma=\frac{\beta_2}{\beta^*}-\frac{\sigma_{\omega2}\kappa^2}{\sqrt{\beta^*}},$$

$$\kappa=0.41,\beta^*=0.09.$$

3 Computational details

3.1 Computational case

Figure 1 shows the dimensions of the revolution body. The model is 517.5 mm in length, and the maximum diameter is

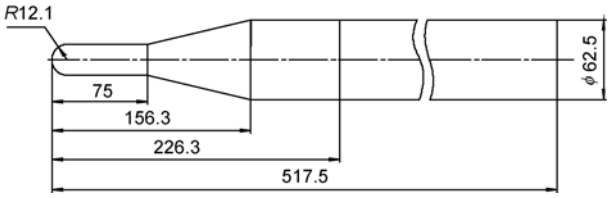

Figure 1 Main dimensions of the revolution body.

62.5 mm. The dimensional parameters of the riblet surface are shown in Figure 2.

3.2 Grids and boundary conditions

The computational domains were meshed using unstructured hybrid grids based on tetrahedral elements and triangular prism elements. The distance between the first layer grids and the wall of the revolution body was determined according to the following equation:

$$\Delta y = \frac{\mu y^+}{\rho u_\tau} = \frac{\nu y^+}{u_\tau}, \tag{12}$$

where u_τ is wall friction velocity, which is given by

$$\overline{C}_f = 2\frac{\rho u_\tau^2}{\rho U_\infty^2} = 2\left(\frac{u_\tau}{U_\infty}\right)^2. \tag{13}$$

Solving eq. (12), we can obtain

$$\Delta y = \frac{\nu y^+}{U_\infty \sqrt{\overline{C}_f / 2}}, \tag{14}$$

where y^+ is the dimensionless distance of the first layer from the wall. The appropriate range of y^+ for the SST k-ω turbulence model is y^+<5; in our simulations, y^+=4. U_∞ is the velocity of external flow, which is calculated by

$$U_\infty = Ma \times \sqrt{kRT} = 278.26 \text{ m/s}, \tag{15}$$

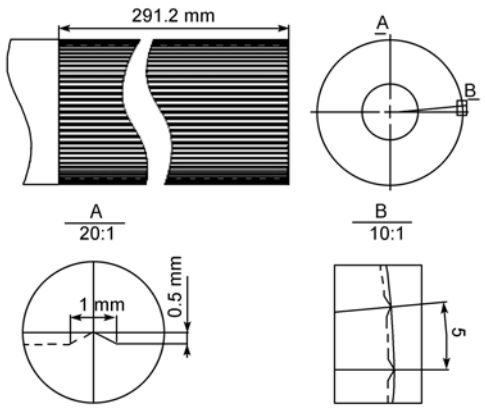

Figure 2 Dimensional parameters of the riblet surface.

where Ma is the Mach number of flow, k the specific heat ratio of air, R gas constant, and T absolute temperature. The values of k and R are 1.4 and 287 m^2/s^2K, respectively.

The average friction coefficient $\overline{C}_f$ can be calculated by the following approximate relationship:

$$\overline{C}_f / 2 = 0.037 Re_L^{-1/5} = 0.001502, \tag{16}$$

where Re_L is the Reynolds number based on length of revolution body, which is defined as

$$Re_L = \frac{U_\infty L}{\nu}, \tag{17}$$

where L is the length of the revolution body, and ν is kinematic viscosity coefficient, which can be defined by

$$\nu = \frac{\mu}{\rho} = \frac{1}{\rho}\left(\frac{T}{288.15}\right)^{1.5}\frac{288.15+C}{T+C}, \tag{18}$$

where T=301.1 K, ρ=1.185 kg/m^3, and C=110.4 K.

Thus, the distance between the first layer grids and the wall of revolution body can be calculated as $\Delta y \approx 0.01$ mm and the boundary layer thickness δ is

$$\delta = 0.035 L Re_L^{-1/7} = 1.835 \text{ mm}. \tag{19}$$

Figure 3 shows the unstructured Cartesian hybrid grids with prismy elements and tetrahedral elements. There are 10 layers of prisms over the surface of the revolution body. The riblet region with high-density grids was provided, which can express the variation of the vortexes forming in the valleys of the two adjacent riblets.

As an axisymmetric body, a quarter of the revolution

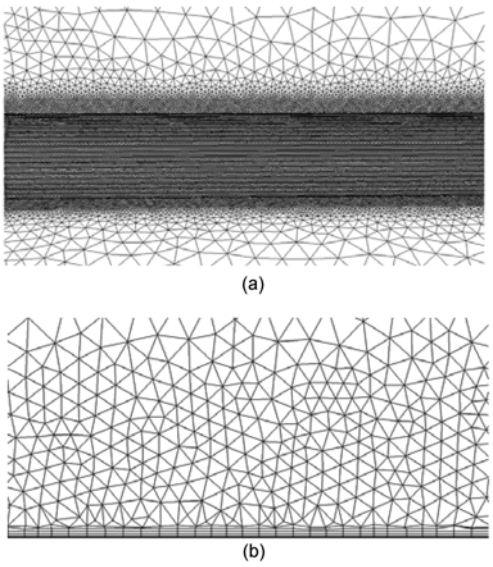

Figure 3 Surface grids and boundary layer grids of bionic riblet region. (a) The surface grids of the riblet region; (b) boundary layer grids near the wall.

body was simulated to reduce the amount of calculation. Thus, the computational domain could be defined as a quarter of a cylinder. The dimensions of the computational domain were $20R_m \times 10L$ (R_m is the maximum radius of the revolution body, L the length of the revolution body).

The pressure of far-field boundary condition was used to model the free-stream compressible at Mach number of 0.8, the gauge pressure of 100460.6 Pa, and the temperature of 301.1 K. The angle of attack was α=0°.

4 Computational results and analysis

4.1 Computational results

The drag reduction rate of the riblet surface is defined as

$$R = \frac{C_{\text{smooth}} - C_{\text{riblet}}}{C_{\text{smooth}}} \times 100\%, \tag{20}$$

where C_{smooth} is the drag coefficient of the smooth revolution body, and C_{riblet} the counterpart of the riblet one. According to eq. (20), the drag reduction rates of the viscous drag, the pressure drag, and the total drag were obtained. The results showed that the riblets reduced the viscous drag of the revolution body by 8.59%, the pressure drag by 8.27%, and the total drag by 9.91%.

4.2 Mechanism of friction drag reduction

The viscous friction stress of the revolution body includes viscous shear stress and turbulent Reynolds stress, defined by

$$\tau = \tau_w + \tau_t = \mu \frac{\partial v_x}{\partial y} + \mu_t \frac{\partial \overline{v}_x}{\partial y}, \tag{21}$$

where μ is dynamic viscosity coefficient, and μ_t is turbulent viscosity coefficient. The relationship of the instantaneous velocity v_x, the time averaged velocity $\overline{v}_x$, and the fluctuation velocity v' is $v_x = \overline{v}_x + v'$. The interpretation of the skin friction drag reduction mechanism should be based on eq. (21).

Figure 4 shows the wall shear stresses of the riblet revolution body and the smooth one. Evidently, the wall shear stress of the riblet region was reduced observably. Figure 5 compares the velocities of the same location near the wall for the riblet and the smooth revolution bodies, which gives the reason of the wall shear stress reduction of the riblet surface. From Figure 5(a) and (b), we can see that the flow speed near the riblet wall is visibly lower than that of the smooth counterpart. In Figure 5(b), δ^+ was defined as

$$\delta^+ = \frac{\Delta y}{\delta}, \tag{22}$$

where Δy is the distance from monitoring point to the wall of the model, and δ the boundary layer thickness. From Figure 5(b), we can deduce that the riblet surface can reduce the velocity gradient of flow field near the wall, and increase the viscous sublayer of the boundary layer. Therefore, the viscous shear stress item of eq. (20) is reduced.

According to the physical origin of Reynolds stress, we know that the speed pulsation intensity can reflect the scale of Reynolds stress. Moreover, the speed pulsation intensity can be expressed by turbulent intensity, which is the ratio of the root mean square of the pulsation speed and the time-averaged velocity. Figure 6 compares the turbulent intensities and the turbulent kinetic energies of the riblet and the smooth revolution bodies. From Figure 6, we can draw that the Reynolds stress is reduced. That is because the turbulent intensity near the riblet surface is lower than that of the smooth counterpart, and the turbulent kinetic energy near the riblet surface consumed by the turbulent fluctuation is lower than that of the smooth surface.

In summary, the bionic riblet surface can reduce the viscous shear stress and the Reynolds stress simultaneously. Therefore, the friction drag of the riblet revolution body can be reduced evidently.

4.3 Mechanism of pressure drag reduction

The pressure drag of the revolution body includes the base drag and the shock wave drag. The base drag can be calculated by

$$C_{AB} = -\frac{p_b - p_\infty}{\frac{1}{2}\rho_\infty U_\infty^2 S_M} \cdot S_b, \tag{23}$$

where S_b is the area of the revolution body base, and S_M is the maximum of the revolution body cross section. Figure 7(a) and (b) compare the base pressures of the riblet and the smooth revolution bodies. The results indicate that the base pressure near the bottom of the riblet is higher than that of the smooth one. Namely, the riblet surface reduces the pressure difference of the revolution body. Accordingly, the pressure drag is reduced remarkably.

4.4 Analysis of turbulent boundary layer control utilizing the riblet surface

Figure 8 compares the streamline on the riblet and smooth surfaces of revolution bodies. Obviously, the streamlines of the riblet revolution body are more uniform than those of the smooth one, indicating that the riblets arranged on the rearward of the revolution body cut the flow near the wall of revolution body. We can deduce that some small second vortexes located inside the valleys of the two adjacent riblets, and the streamwise vortices flow through the revolution body over the second vortexes. Finally, we can

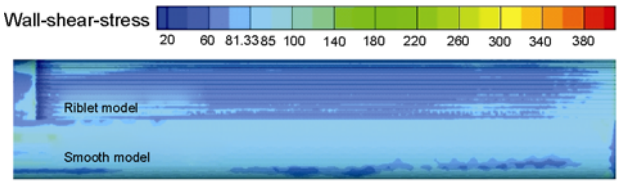

Figure 4 Comparison of the wall shear stresses for the riblet and the smooth revolution bodies.

conclude that the spanwise vortices are suppressed, and the streamwise velocity fluctuations are decreased.

The small second vortices produced in the valleys of the two adjacent riblets increase the distance between the streamwise vortices and the wall of revolution body, then increase the boundary layer thickness, and finally weaken the pumping action on the dead water region behind the revolution body caused by the external flow.

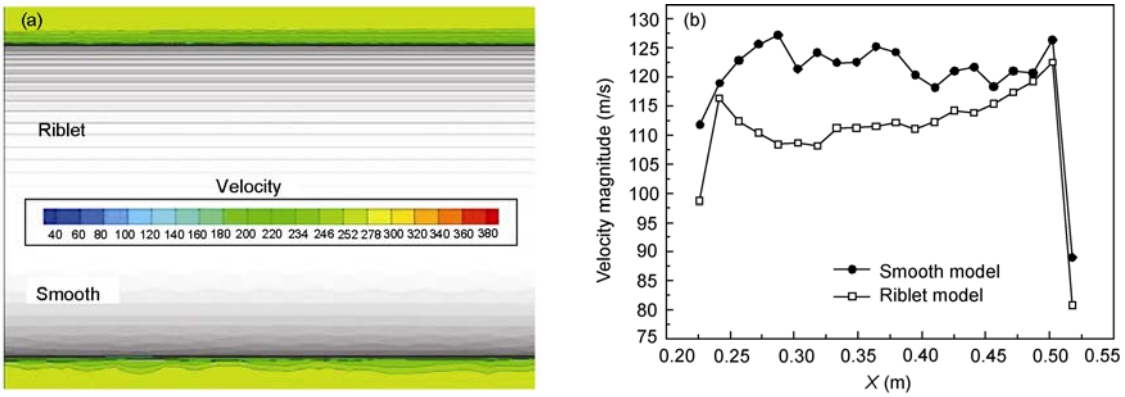

Figure 5 Comparison of the velocities near the wall for the riblet and the smooth revolution bodies. (a) Contour of velocity; (b) velocity of the same location.

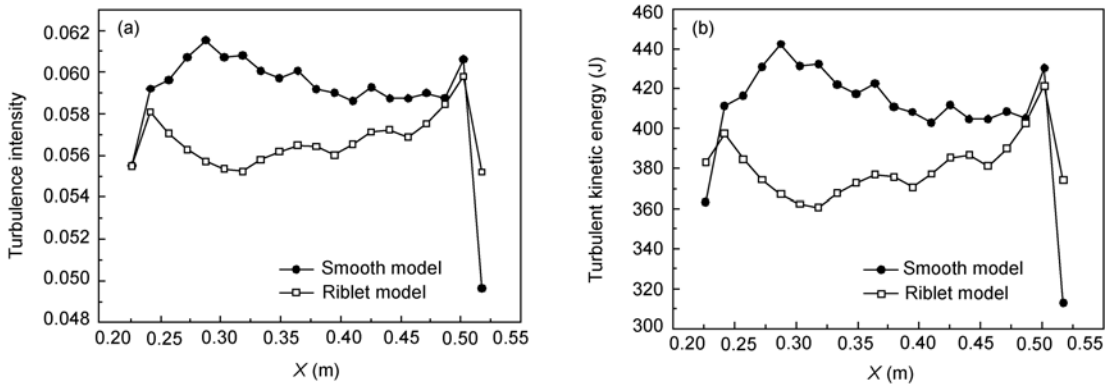

Figure 6 Comparison of turbulent intensities and turbulent kinetic energies of the riblet and the smooth revolution bodies. (a) Turbulent intensities; (b) turbulent kinetic energies.

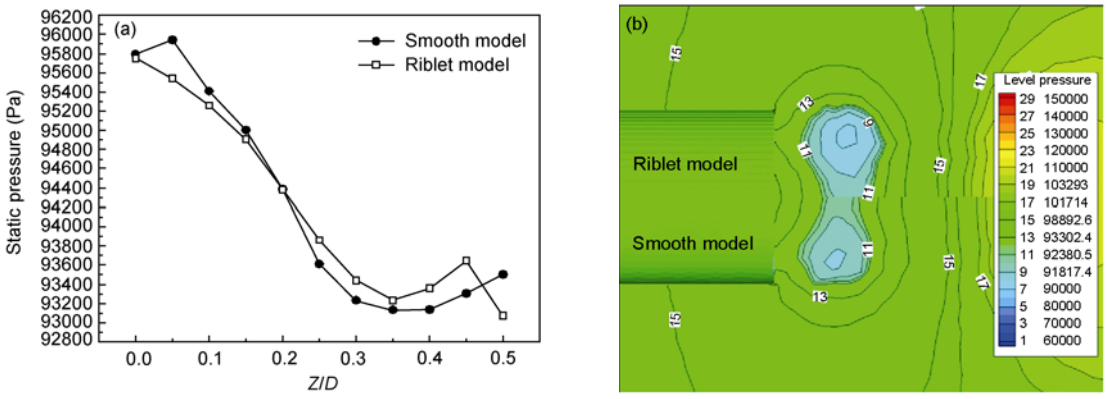

Figure 7 Comparison of the base static pressures for the riblet and the smooth revolution bodies. (a) Base static pressures of the revolution bodies (D is the diameter of the revolution body); (b) Contours of static pressure.

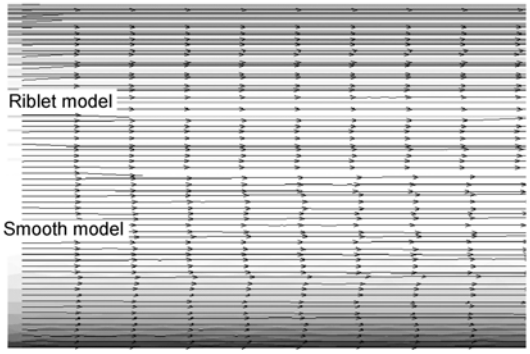

Figure 8 Comparison of wall trace lines for the riblet and the smooth revolution bodies (*Ma*=0.8).

5 Conclusions

In the view of the results of the presented numerical simulation with the SST k-ω model, the following conclusions are drawn.

(1) At the Mach number of 0.8, the riblet surface arranged on the rearward of the revolution body can reduce the viscous drag by 8.27%, the pressure by 9.91%, and the total drag by 8.59% in the synthesis.

(2) The basic reason of the reduction of skin friction drag is that the riblet surface controls and corrects the boundary layer. In a word, the spanwise vortices are suppressed, and the turbulence burst strength is decreased. Therefore, the two drag elements composing the skin friction drag are simultaneously reduced.

(3) The mechanism of the pressure drag reduction is that the riblet surface weakens the pumping action on the dead water region behind the revolution body caused by the external flow.

This work was supported by the Base Platform Construction Project of Jilin University Basic Scientific Research (Grant No. 421060202466), the Technology Development Plan Project of Jilin Province (Grant No. 20096032), the Youth Research Foundation of the Jilin University Agronomy Faculty (Grant No. 4305050102k7), the Key Program of National Natural Science Foundation of China (Grant No. 50635030), and the Major Program of the Science and Technology Development of Jilin Province (Grant No. 09ZDGG001).

1 Walsh M J, Michael J. Riblets as a viscous drag reduction technique. AIAA J (S1533-385X), 1983, 21: 485–486
2 Reif W E, Dinkelacker A. Hydrodynamics of the squamation in fast swimming sharks. Neues Jahrb Geol Paläontologie (S0077-7749), 1982, 164: 184–187
3 Bechert D W, Hoppe G, Reif W E. On drag reduction of the shark skin. AIAA paper, 1985, 85: 546
4 Bechert D W, Bruse M, Hage W. Experiment with three-dimensional riblets as an idealized model of shark skin. Exp Fluids, 2000, 28: 403–412
5 Fish F E, Battle J M. Hydrodynamic design of the humpback whale flipper. J Morphol (S0362-2525), 1995, 225: 51–60
6 Miklosovic D S, Murray M M, Howle L E, et al. Leading edge tubercles delay stall on humpback whale (Megaptera Novaeangliae) flippers. Phys Fluids (S1070-6631), 2004, 16: 39–42
7 Anderson E J, MacGillivray P S, DeMont M E. Scallop shells exhibit optimization of riblet dimensions for drag reduction. Biolog Bull (S0006-3185), 1997, 192: 341–344
8 Luchini P, Manzo F, Pozzi A. Resistance of a grooved surface to parallel flow and cross flow. J Fluid Mech, 1991, 228: 87–109
9 Choi H, Moin P, Kim J. Direct numerical simulation of turbulent flow over riblets. J Fluid Mech, 1993, 255: 503–539
10 Wang J J, Lan S L, Chen G. Experimental study on the turbulent boundary layer flow over riblets surface. Fluid Dynam Res, 2000, 27: 217–229
11 Goldstein D, Handler R, Sirovich L. Direct numerical simulation of turbulent flow over a modeled riblet covered surface. J Fluid Mech, 1995, 302: 333–376
12 Ren L Q, Zhang C C, Tian L M. Experiment study on drag reduction for bodies of revolution using bionic non-smoothness. J Jilin U, 2005, 35: 431–436
13 Zhang C C, Ren L Q, Liu Q P, et al. Experimental study on bionic dimpled surfaces of bodies of revolution for drag reduction. ACTA Aerodynamica Sinica, 2008, 26: 79–84
14 Menter F R. Two-equation eddy-viscosity models for engineering applications. AIAA J (S1533-385X), 1994, 32: 1598–1605
15 Pietro C, Marcello A. An evaluation of RANS turbulence modelling for aerodynamic applications. Aeros Sci Tech (S1270-9638), 2003, 7: 493–509